UC Berkeley

UC Berkeley Previously Published Works

Title

A photochargeable semiconductor for highly efficient dehydrogenative coupling of amines

Permalink

https://escholarship.org/uc/item/3c29z0n9

Journal

Nature Chemistry, 18(6)

ISSN

1755-4330

Authors

Luo, Jie

Chen, Xinyu

Jayasinghe, Lihini

et al.

Publication Date

2026-06-01

DOI

10.1038/s41557-026-02109-6

Copyright Information

This work is made available under the terms of a Creative Commons Attribution License, available at https://creativecommons.org/licenses/by/4.0/

Peer reviewed

eScholarship.org Powered by the California Digital Library
University of California

Photochargeable semiconductor for highly efficient dehydrogenative coupling of amines

Jie Luo,[1,2,†,‡] Xinyu Chen,[1,2,†] Lihini Jayasinghe,[1,†] Nathan Edward Soland,[1] Yu Shan,[3,4] Arifin Luthfi Maulana,[2,3] Heqing Zhu,[1,6] Maria Fonseca Guzman,[1] Alexander M. Oddo,[1,5] Kiran M. Donnelly,[1] Jihoon Choi,[3] Julian Feijoo,[1] Bernd Schaefer,[7] Matthias Schmalzbauer,[7] Rui Zhang,[2] Fabian Seeler,[7] Carlos Lizandara-Pueyo,[2,7] Richard D. Schaller,[8,9] Peidong Yang[1,2,3,4,5,6,*]

1 Department of Chemistry, University of California, Berkeley, California 94720, United States. 2 California Research Alliance (CARA), BASF Corporation, Berkeley, California 94720, United States. 3 Department of Materials Science and Engineering, University of California, Berkeley, California 94720, United States. 4 Chemical Sciences Division, Lawrence Berkeley National Laboratory, Berkeley, California 94720, United States. 5 Kavli Energy NanoScience Institute, Berkeley, California 94720, United States. 6 Materials Sciences Division, Lawrence Berkeley National Laboratory, Berkeley, California 94720, United States. 7 BASF SE, 67056 Ludwigshafen am Rhein, Germany. 8 Department of Chemistry, International Institute for Nanotechnology, Northwestern University, Evanston, Illinois 60208, United States. 9 Center for Nanoscale Materials, Argonne National Laboratory, Lemont, Illinois 60439, United States.

†J.L., X.C., L.J. contributed equally

‡Current address: Department of Chemistry, Zhejiang University, Hangzhou 310058, China.

*E-mail: p_yang@berkeley.edu

The development of materials with high photocatalytic efficiency is essential for sustainable chemical transformations. Here, we introduce photochargeable zinc indium sulfide nanocrystals (ZIS NCs) with notable charge storage capacity, enabling highly efficient photocatalytic dehydrogenative coupling of amines. Combined with a nickel cocatalyst, ZIS NCs deliver diamines and hydrogen at rates exceeding 120 mmol per gram of photocatalyst per hour, with >95% selectivity and an apparent quantum efficiency of 39.4% under ambient conditions. The system exhibits excellent scalability, demonstrated by a 20-gram scale reaction, and broad versatility in promoting amino acid ester coupling and polymerization reactions with concurrent hydrogen evolution. Mechanistic studies attribute the photocharging capability of ZIS NCs to *in situ* generated trap states such as sulfur vacancies, which extend hydrogen production into the dark catalytic cycle and significantly enhance the overall charge utilization efficiency. These findings position photochargeable semiconductors as promising platforms for a wide range of photocatalytic applications.

The Calvin cycle, a central component of natural photosynthesis, produces carbohydrates using NADPH and ATP generated by the coordinated activity of Photosystem I (PSI) and Photosystem II (PSII).[1] Although classified as part of photosynthesis, the Calvin cycle operates as a light-independent process, functioning without direct illumination. This intricate biochemical system has inspired efforts to mimic its mechanisms, advancing light harvesting and energy utilization in photocatalytic systems.[2] A promising strategy in this pursuit involves the development of photochargeable semiconductors—materials uniquely capable of storing photoexcited charges like batteries,[3-5] and driving chemical reactions without continuous light exposure. This phenomenon is commonly referred to as dark photocatalysis or persistent photocatalysis.[6-10] An often underappreciated intrinsic advantage of these materials is their ability to decouple charge utilization.[10] By selectively storing photoinduced charges within their structure (e.g., electrons), they minimize charge recombination—a primary efficiency-limiting factor in conventional semiconductor photocatalysis (Fig. 1).[11,12] This characteristic provides a compelling platform for photocatalytic systems with enhanced efficiency and effectively extends the reaction window of photocatalysis.

In this study, we report the application of photochargeable semiconductor for the efficient and sustainable production of diamines. Diamines are fundamental building blocks in the production of polymers such as polyamides, epoxy resins, and polyurethanes due to the bifunctional charateristics.[13,14] However, traditional synthetic methods for diamines, including reductive amination and condensation, generate a lot of waste, are subject to harsh conditions, and use toxic reagents, which raises environmental concerns.[15,16] In this context, photocatalytic dehydrogenative coupling of readily available amines has emerged as a sustainable alternative, offering an atom-economical route to diamine production while generating hydrogen gas as the sole, intrinsically valuable byproduct.[17-20] Nevertheless, existing photocatalytic approaches are often limited by low efficiency, poor selectivity, and inadequate scalability, hindering broader industrial adoption.[21-25]

We demonstrate that zinc indium sulfide nanocrystals (ZIS NCs), recently developed by our group,[26] exhibit pronounced photochargeable behavior in the dehydrogenative coupling of amines. When combined with nickel as a hydrogen evolution cocatalyst, as established in our previous work, the system delivers outstanding photocatalytic performance. It achieves diamine production rates exceeding 120 mmol per gram of photocatalyst per hour (mmol g^{-1} h^{-1}), with >95% selectivity and an apparent quantum efficiency (AQE) of up to 39.4% under ambient conditions. It also demonstrates practical scalability, with successful catalyst recycling over six cycles and reaction scaling to over 20 grams. Furthermore, the platform facilitates the coupling and polymerization of amino acid esters, highlighting its potential for the sustainable synthesis of diverse and valuable chemical products.

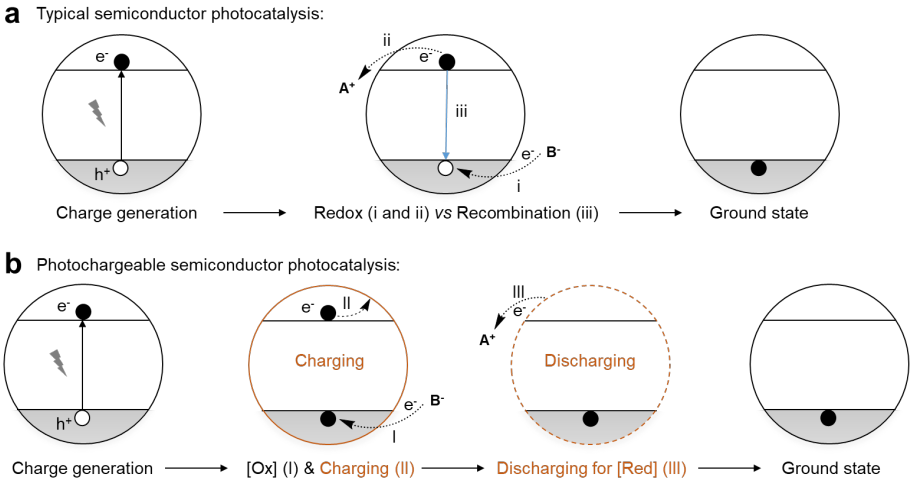


Fig. 1 | Photochargeable semiconductor for enhanced photocatalysis. a, In conventional semiconductors, photogenerated charges follow three competing pathways: i, electron transfer to drive reduction reactions; ii, hole transfer to drive oxidation reactions; and iii, electron–hole recombination. All occur on the ps–µs timescale, with recombination limiting catalytic efficiency. **b**, In photochargeable semiconductors, charge pathways are decoupled: I, photogenerated holes rapidly oxidize substrates; II, photoelectrons are stored within the structure; and III, the stored electrons are subsequently utilized for delayed reduction reactions (up to minutes), thereby suppressing recombination losses.

Results

Establishment of photocatalysis. α-Methylbenzylamine **1a** was selected as the model substrate to evaluate the feasibility of ZIS NCs in promoting the coupling reaction.[26] This reaction is designed to produce a sterically hindered diamine **2a**, a class of compounds particularly valued for their ability to enhance polymer flexibility and thermal resistance while reducing crystallinity—key features for the development of materials with tailored properties.[27-29] Moreover, the presence of two primary amine groups in **2a** makes it highly suitable for potential polymer applications.

Our ZIS NCs exhibited excellent selectivity (>95%) for diamine generation, achieving a production rate of 65 mmol g^{-1} h^{-1} within the first 3 h of the reaction (Fig. 2a and S1). The addition of nickel markedly enhanced the catalytic efficiency,[30] enabling full amine conversion and boosting the diamine production rate to over 120 mmol g^{-1} h^{-1} with just 1 wt % Ni^{2+} relative to the photocatalyst—this is 13 times higher than the best-reported result to date (Fig. S2-S4).[24] This enhancement arises from the role of Ni as a hydrogen evolution cocatalyst, deposited *in situ* by photoreduction of Ni^{2+} with ZIS photoelectrons on the ZIS NC surfaces (Extended data Fig. 1, Fig. S5 and Supplementary Note 1).[31] Further increasing the nickel loading to 3 wt % maintains the activity, and a decrease in both selectivity and efficiency was observed when the loading was raised to 12 wt %. Other common cocatalysts, such as platinum and palladium, maintained decent selectivity but underperformed compared to nickel regarding catalytic activity.

The reaction was monitored over time, revealing a steady accumulation of the desired diamine product alongside hydrogen evolution and the gradual consumption of the substrate (Fig. 2b). Notably, no significant side products were detected, including the commonly observed imine—which is readily accessible by other methods,[21,22,32] indicating a clean and efficient process that simplifies product isolation. The practicality of this system was further demonstrated through catalyst recycling and reuse tests (Fig. S6 and S7). As shown in Fig. 2c, starting with just 2 mg of ZIS NCs with nickel as the cocatalyst, the photocatalyst was successfully recycled and reused for six cycles (6 × 7.7 mmol), maintaining excellent conversion and decent selectivity throughout. Additionally, the synthesis of ZIS NCs and the catalytic experiments were easily scalable (Fig. 2d). We achieved a 10-fold scale-up of the ZIS NC synthesis, yielding 1.7 g of photocatalyst per batch (Fig. S8). The catalytic reaction was similarly scaled up to a 20 mL substrate volume (155 mmol), yielding 17.3 g of isolated diamine and generating 1.8 L of green hydrogen gas (Fig. S9 and S10). These scale-up experiments underscore the robustness and scalability of the developed system, positioning it as a promising candidate for industrial applications.

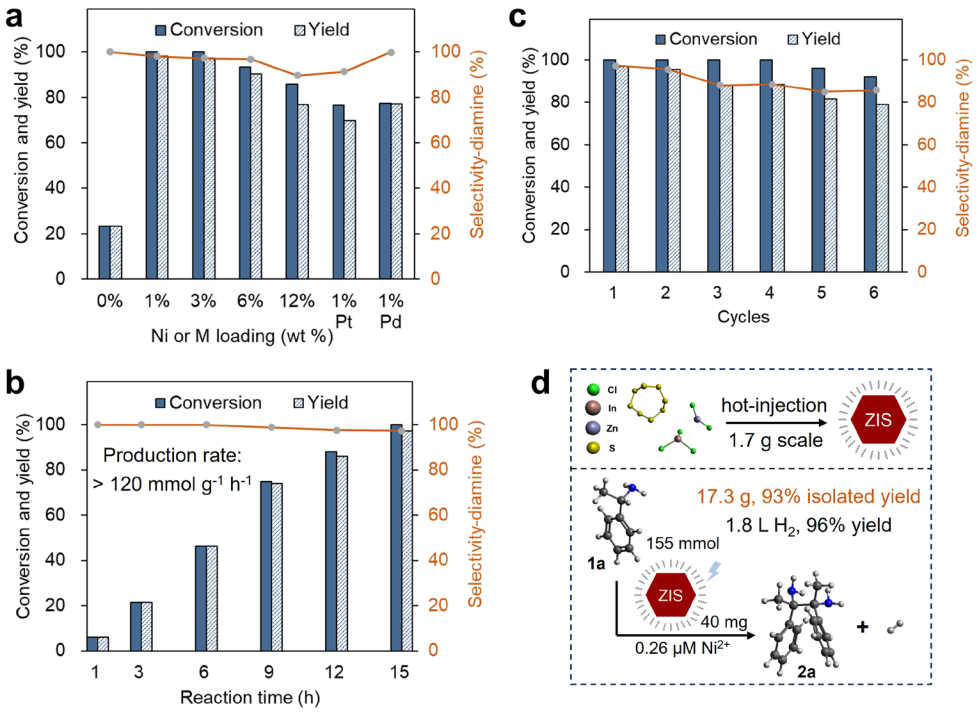


Fig. 2 | Photocatalytic dehydrogenative coupling of amines. a, Cocatalyst tests. **b**, Reaction progress monitoring. **c**, Catalyst recycling and reuse test. **d**, Scaled-up synthesis of ZIS NCs and catalytic reactions. General exploration was carried out with 2 mg photocatalyst under air-free conditions with 1 mL of **1a** in DMF under a 370 nm UV light (30 mW/cm^2, Kessil lamp) for 15 h, and the selectivity was calculated on a carbon basis. Due to the large volume of hydrogen generated (typically 88±2 mL), it was released into the hood unless intentionally collected using a eudiometer. All experiments, including scale-up syntheses, were performed in duplicate.

Photocharging behavior of ZIS NCs. During our investigation of the reaction, we observed that hydrogen evolution persisted for more than 15 minutes after the light source was turned off (Fig. 3a). Controlled experiments confirmed that the post-illumination hydrogen gas did not originate from hydrogen trapped in the reactor walls or dissolved in the solution, indicating the occurrence of a dark reaction. This phenomenon was observed with both nickel and platinum cocatalysts (Fig. S11), suggesting that it is independent of the specific cocatalyst used. Notably, the post-illumination effect was more pronounced in scaled-up reactions using 40 mg of ZIS NCs catalyst. On average, approximately 4 mL of hydrogen gas (0.16 mmol) was collected in the dark after illumination (Fig. S12), vastly exceeding the total amount of cocatalyst present (0.02 mmol, 3 wt %). This effectively rules out hydrogen generation originating solely from a chemical reaction between the reduced cocatalysts and released protons (H^+).

An alternative explanation is that photogenerated electrons persist in ZIS NCs even in the absence of light, enabling dark hydrogen evolution via proton reduction. To validate this hypothesis, ferricyanide [$Fe(CN)_6^{3-}$], an electron scavenger, was introduced one minute after the light source was turned off. As shown in Fig. 3b, the characteristic absorption of $Fe(CN)_6^{3-}$ at 420 nm disappeared upon mixing with the reaction mixture. Quantitative titration experiments revealed that 6.7 μmol of electrons were consumed by 2 mg of ZIS after irradiation—approximately half of the hydrogen evolved in the corresponding dark reaction (Fig. S13 and S14)[33]—thereby confirming the presence of residual electrons post illumination. This charged state likely arises from the rapid trapping of photogenerated electrons, facilitated by the concurrent fast consumption of holes by reductants or ligands (Extended data Fig. 2).[34] The retention of these electrons suggests that electron-hole recombination is significantly suppressed, allowing the semiconductor to maintain a photocharged state with enhanced charge separation. This suppression likely accounts for the high AQE of up to 39.4% observed under current conditions (Fig. 3c).

UV–Vis spectroscopy was employed to further probe the photocharging behavior of ZIS NCs. Upon illumination, the absorption spectrum of the ZIS dispersion exhibited a broad increase associated with nickel photodeposition, accompanied by the disappearance of the first excitonic absorption band (Fig. 3d). Notably, the original spectral profile was fully restored upon exposure of the mixture to air, indicating that the bleaching arises from conduction band filling by photogenerated electrons, which are subsequently removed by oxygen (Fig. S14–S17). Similar phenomenon has been reported in quantum dots such as CdSe and CdS, but this represents the first observation for ZIS NCs.[35-38] However, quantitative electron-counting experiments reveal that the number of stored electrons far exceeds the expected conduction band capacity (Supplementary Note 2),[34] and since multiexciton generation is improbable under the excitation wavelength used, the excess electrons must be stored in additional, deeper trap states.[37,39]

Kinetic measurements further reinforce the presence of such long-lived trapped electrons. The photocharged ZIS shows an initial rapid decay within the first five minutes, followed by a pronounced, long-lived component that persists for tens of minutes—mirroring the timescale of dark hydrogen evolution. This temporal correlation confirms that the material maintains a stable photocharged state well after illumination ceases. Transient absorption (TA) spectroscopy, particularly analysis of the ground-state bleach (GSB) recovery (Fig. 3f), reveals a pronounced reorganization of carrier dynamics upon addition of amine (Fig. 3g). Pristine ZIS displays a relatively slow and monotonic GSB recovery extending into the multi-nanosecond regime (Fig. S19), consistent with recombination through surface and deep trap states. In contrast, introducing the amine accelerates the early-time recovery and substantially reduces the overall GSB amplitude, indicating rapid extraction of photogenerated electrons by the amine. Most notably, the amine-treated sample exhibits a pronounced long-lived tail that persists out to ~7 ns, reflecting the formation of a deeply trapped, charge-separated state that is absent or much less prominent in pristine ZIS. This redistribution of the carrier population into a long-lived reservoir provides direct kinetic evidence of photocharging in ZIS. Similar behavior was observed when Ni was introduced as a cocatalyst (Fig. S20). Consistent with this behavior, both steady-state and time-resolved photoluminescence measurements point to the presence of deep electron traps (Extended data Fig. 3). EPR spectroscopy was then employed to directly probe the trapped electrons associated with defect states (Fig. 3h). Relative to defect-free ZIS (Fig. S21), the pristine ZIS NC powder exhibited a pronounced EPR signal characteristic of sulfur vacancies,[40,41] consistent with the deep trap states inferred from TA and PL measurements. Although these vacancies can be passivated through ligand exchange with sulfide anions, they readily regenerate under photocatalytic conditions.[42]

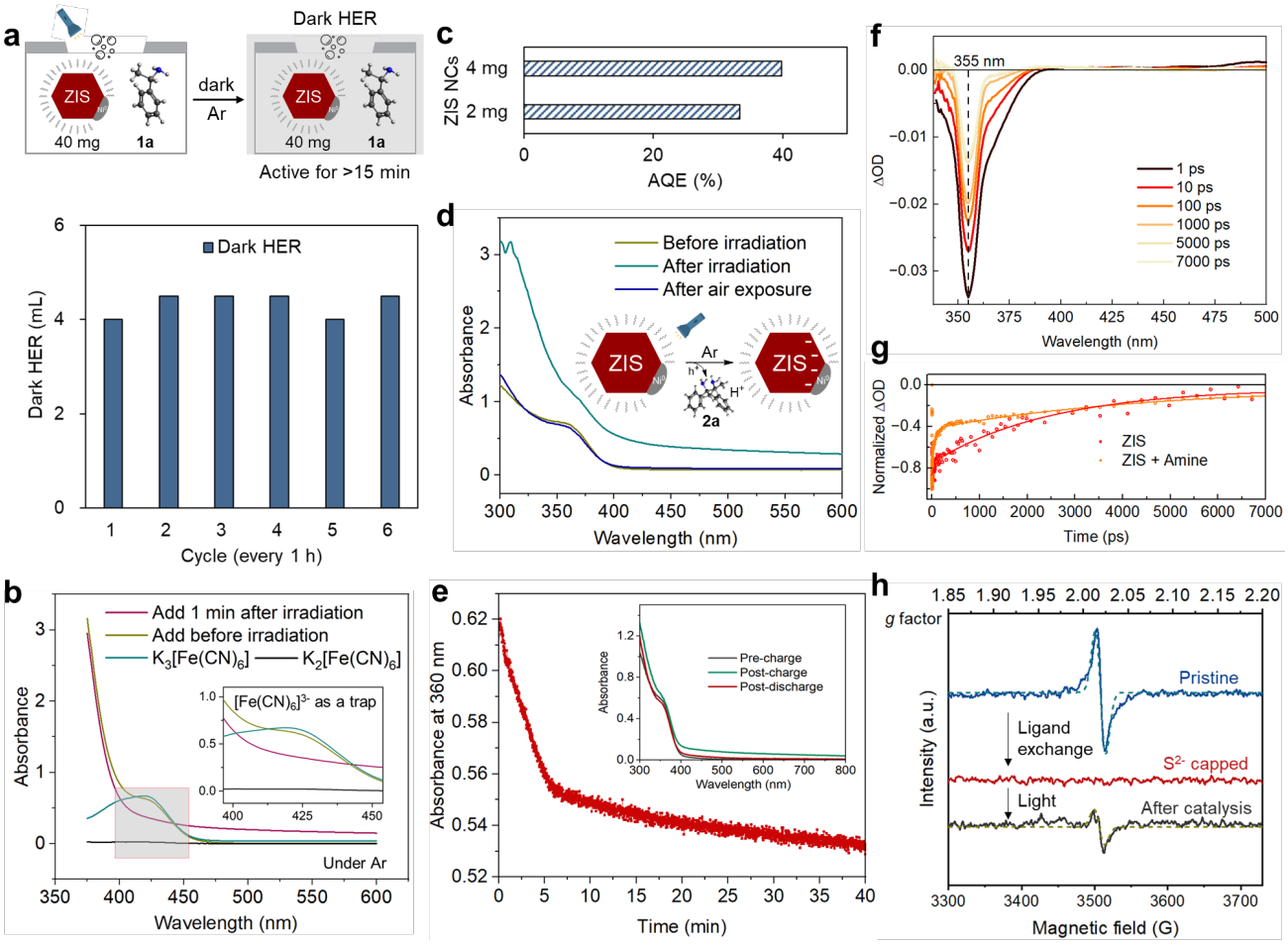


Fig. 3 | Photocharging behavior of ZIS NCs enables post-illumination reactions. a, Hydrogen evolution observed post-illumination (dark hydrogen). **b**, Use of the electron trap reagent $K_3[Fe(CN)_6]$ to confirm the presence of photogenerated electrons after the illumination was off. **c**, Apparent quantum efficiency (AQE) measured during the first six hours of the reaction using varying amounts of ZIS NCs under 370 nm UV light (5.3 cm², 30 mW/cm²). **d**, UV-Vis spectra of ZIS NC dispersion showing changes after illumination and subsequent restoration upon air exposure, indicating the photocharged state. **e**, Monitoring of the discharging process by kinetic UV–Vis absorption at 360 nm. Inset: Steady-state spectra of the photocharging process. **f**, TA spectra of the photocatalytic system following 355 nm excitation (85 μW), collected from ps to ns. **g**, Normalized GSB decay kinetics extracted at 355 nm. **h**, Electron paramagnetic resonance (EPR) study of ZIS NCs powder, revealing unpaired electrons associated with sulfur vacancies. The dotted line corresponds to the simulated signal of sulfur-vacancy for comparison.

To further elucidate the structural evolution accompanying photocharging, operando X-ray absorption spectroscopy (XAS) was conducted. While XANES analysis showed that the formal oxidation states of Zn^{2+} and In^{3+} remain unchanged during illumination (Fig. 4a and 4c), operando EXAFS revealed substantial light-induced perturbations in the metal–sulfur coordination environment, including an 40% loss of total In–S coordination (Fig. 4b and 4d, Extended data Table 1 and Fig. S22-27). This significant reduction provides direct evidence for the *in situ* generation of sulfur vacancies (Fig. 3h and S28) and can quantitatively account for most of the stored electrons, assuming that cleavage of each In–S bond accommodates approximately two electrons (Supplementary Note 2).[43,44] The resulting trapped electrons can be further stabilized by proton intercalation within the layered ZIS framework,[45-47] aided by protons generated in the reaction medium during catalysis (Fig. 4e). Notably, this unusually high charge-storage capacity originates from the single-plate architecture of the ZIS NCs, which exposes a large fraction of surface sulfur atoms and creates a dense array of chemically addressable trapping sites. The resulting *in situ* generated electron traps effectively deplete the conduction band (Fig. 4f-ii; Extended data Fig. 2), sustaining light absorption and suppressing charge recombination. Together, these factors account for the exceptional photocatalytic efficiency observed in this system.

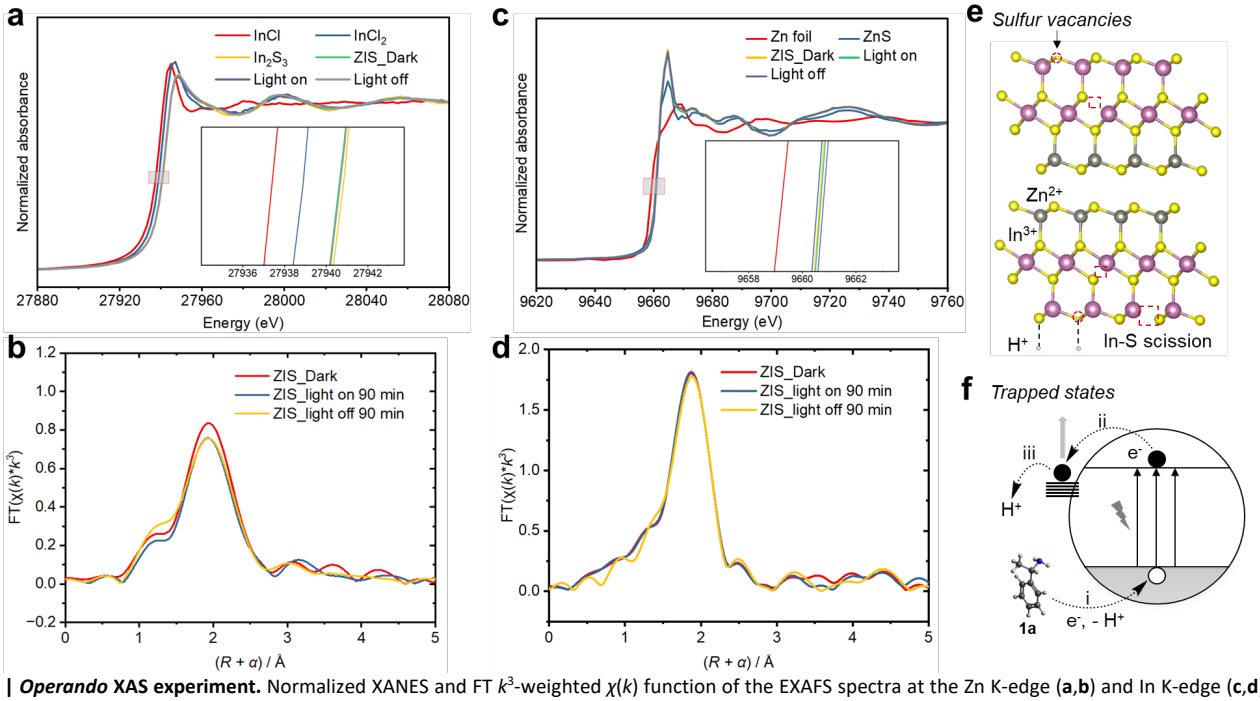


Fig. 4 | *Operando* XAS experiment. Normalized XANES and FT k^3-weighted $\chi(k)$ function of the EXAFS spectra at the Zn K-edge (**a**,**b**) and In K-edge (**c**,**d**). **e**, Schematic illustration of sulfur vacancies (red dotted circles) and cleaved In-S bonds in the crystal structure, acting as electron traps for charge storage. **f**, Schematic illustration of hole consumption by amines and the electron traps for storage.

Probing molecular pathways of the reaction. The generation of the diamine product suggests the involvement of an aminocarbon radical intermediate. To elucidate the reaction mechanism, *in situ* EPR spectroscopy studies were conducted using the catalytic solution with 5,5-dimethyl-1-pyrroline-N-oxide (DMPO) as a spin-trapping agent (Fig. 5a). Upon light illumination, distinct signals corresponding to carbon-DMPO type radical adducts were observed, providing direct evidence for the generation of aminocarbon radicals as key intermediates (Fig. S29).[17] These intermediates are responsible for the high selectivity observed in diamine production. In contrast, when 1,1-diphenylethylene was introduced as a slower-reacting radical trap,[48] no detectable radical intermediates were captured (Fig. S30). This suggests that aminocarbon radicals derived from α-methylbenzylamine are rapidly consumed, likely undergoing self-coupling on the surface of ZIS NCs to form the diamine product. This process may be facilitated by the interaction between amines and the ZIS NCs, which promotes preorganization of the amines for the reaction (Extended data Fig. 4).[49]

While aminocarbon radicals were identified as the primary radical species, control experiments using protonated or acetylated amine substrates exhibited no reactivity under the photocatalytic conditions (Fig. 5b). This underscores the critical role of the free amino group in enabling the reaction, suggesting an indirect oxidative deprotonation process for the generation of the aminocarbon radical.[50] This process likely begins with the formation of amino cation radicals, followed by α-proton deprotonation, which is further facilitated by the tethered phenyl group (see Supplementary Note 3 for the effect of the conjugation group). Additional support for this hypothesis comes from experiments with aliphatic amines, where nitrogen-centered radical species were observed upon light illumination (Fig. S31).

Based on these findings, a mechanism for diamine formation is proposed (Fig. 5c, i-v). Upon light illumination, electron-hole pairs are generated within the ZIS NCs and migrate to their surface for redox processes (i). The photogenerated holes oxidize amine molecules which bind to the catalyst surface, forming aminocarbon radicals and releasing protons (ii). These radicals then rapidly couple with each other on the surface of ZIS NCs to yield the diamine product (iii). Meanwhile, the ZIS NCs remain in a photocharged state, with the stored electrons driving proton reduction for hydrogen evolution—a process further accelerated by the nickel cocatalyst, even after light is turned off (iv). New amine molecules subsequently exchange with the generated diamine on the surface, ensuring sustained catalyst turnover and maintaining high reaction efficiency (v).

Interestingly, while imines are commonly observed in other photocatalytic systems,[21,22,32] their generation in this system is reversible. For example, when imine was used as the starting material, diamine and aminoalcohol products were observed (Fig. 5d and Fig. S32). These products are formed via reductive coupling of the imine through the aminocarbon radical intermediate.[15] This reactivity can be attributed to the highly reducing nature of the photogenerated electrons, a consequence of quantum confinement effects in the ZIS NCs (Fig. S33 and S34).[26] These electrons can reduce imines back to aminocarbon radicals, further enhancing the system's excellent selectivity for diamine generation as an irreversible product (Supplementary note 4).

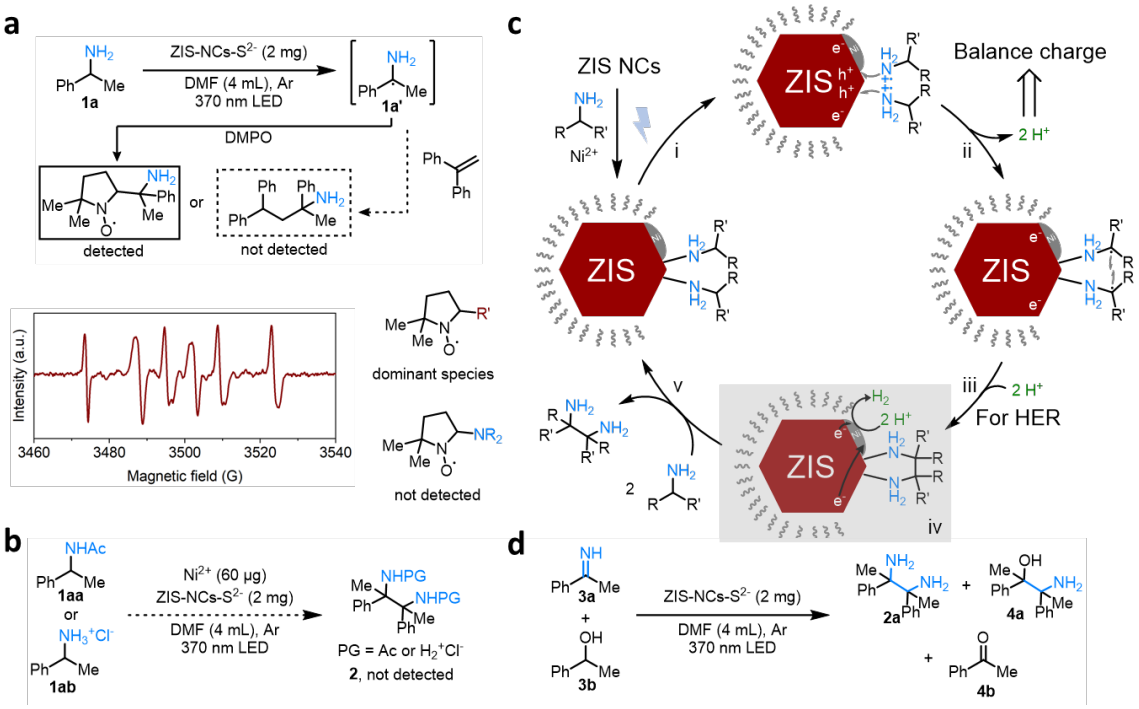


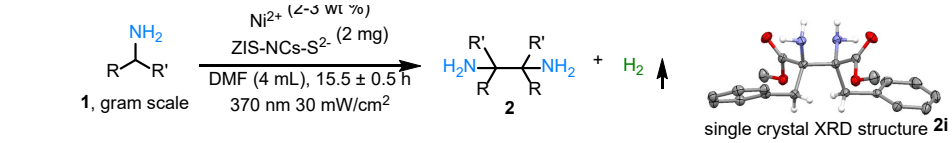
Fig. 5 | Probing molecular pathways and the proposed mechanism. a, *In situ* EPR spectra taken during the photocatalytic reaction in the presence of DMPO as a spin-trapping agent under light irradiation and radical trapping experiments using 1,1-diphenyl ethylene as the reagent. **b**, Control experiments using protonated or acetylated amine substrates. **c**, Proposed molecular mechanism for diamine generation through photocatalytic dehydrogenative coupling of amines. **d**, Reductive coupling of imines renders high selectivity towards diamines.

Substrate scope. With the developed photocatalytic system in hand, we systematically investigated the reaction scope, with particular emphasis on primary amines capable of producing sterically hindered diamine products (Fig. 6). Remarkably, most aryl amines, including those with significant steric hindrance, achieved complete conversion and excellent selectivity toward the desired diamines (**1a**-**1e**, 86%-95% yields), along with hydrogen evolution. However, the system proved unsuitable for aliphatic amines, such as cyclohexylamine **1f**, which predominantly yielded imine products. This behavior is likely due to the instability of aminocarbon radical intermediates, as evidenced by EPR (see Fig. S31, S35 and Supplementary Note 3).

Interestingly, amino acids emerged as promising substrates for the formation of targeted diamine products, presumably due to the stabilizing effect of their alpha carbonyl group. Nonetheless, when water was employed as the solvent to address the poor solubility of amino acids in DMF, side reactions such as the hydrolysis of the amino group were observed. To mitigate this issue, amino acid esters, which are more soluble in DMF, were utilized. These esters exhibited excellent activity and selectivity for diamine production. For instance, alanine octyl ester **1g** was tested on a 20-gram scale, delivering the corresponding diamine product with high efficiency and selectivity, achieving a 96% yield. Additionally, amino acid esters featuring functional groups such as phenyl, thioether, and phenol were also successfully transformed into the desired diamines with high efficiency (**2h**-**2k**, 95%-98% yields). The structure of the generated diamine product was further validated through the single-crystal XRD analysis of **2i** (Fig. S34). We also tested the coupling of leucine amide **1l**, a model substrate for peptides

and proteins, and found that it performed well in the reaction, suggesting the potential of this methodology for biochemical applications. To the best of our knowledge, this is the first example regarding the dehydrogenative coupling of amino acid derivatives, further expanding the diamine category from a renewable source.

Additionally, the system demonstrated versatility beyond primary amines, proving effective for secondary and tertiary amines. Substrates such as proline ester **1m** and dimethylamino acetonitrile **1n** were efficiently converted into their respective dimers (70% and 89% yields). Notably, the dinitrile product **2n** exemplifies the system's ability to generate other bifunctional products, broadening its utility for complex transformations. Finally, dehydrogenative polymerization was demonstrated using **1o** as the starting material, yielding a polymer with a number-average molecular weight (M_n) of ~12000 as determined by NMR (Fig. S35). This capability illustrates the method's potential for diverse chemical transformations, from small-molecule coupling to polymer synthesis, opening new opportunities for its application in complex catalytic processes.



Primary amines	Conversion	Isolated yield	Primary amines	Conversion	Isolated yield
(**1a**, 20 mL)	>99%	95%	(**1g**, 21 g)	>99%	96%
(**1b**, 1 mL)	>99%	86%	(**1h**, 1 g)	>99%	97%
(**1c**, 1 mL)	>99%	92%	(**1i**, 1 g)	>99%	95%
(**1d**, 1 mL)	>99%	91%	(**1j**, 1 g)	>99%	98%
(**1e**, 0.5 mL)	>99%	87%	(**1k**, 0.5 g)	>99%	96%
(**1f**, 1 mL)	30%[a]	n.d.[b]	(**1l**, 0.5 g)	>99%	86%

Secondary and tertiary amines

(**1m**, 1 g) → >99% conv., **2m**, 70% yield[c] + H_2

(**1n**, 0.5 mL) → >99% conv., **2n**, 89% yield + H_2

Dehydrogenative polymerization

(**1o**, 1 mmol) → **2o**, 94% yield, M_n = ~12000 + H_2

Fig. 6 | Substrate scope of photocatalytic dehydrogenative coupling of amines and dehydrogenative polymerization. Reaction conditions are similar with those described in Fig. 1. **a**, Determined by NMR. **b**, Imine was generated as the major product. **c**, Side reactions on the proline ring were observed.

Conclusions

We present a highly efficient photocatalytic system for the dehydrogenative coupling of amines, offering a sustainable and scalable approach to diamine synthesis, with hydrogen as the only byproduct. Leveraging ZIS NCs as the semiconductor photocatalyst and nickel as a cocatalyst, the system delivers outstanding catalytic performance, achieving highest production

rates of diamines with excellent selectivity and 39.4% AQE under ambient conditions. This remarkable efficiency is expected from the high electron capacity of photochargeable ZIS NCs, which facilitates improved photon absorption and charge utilization. Furthermore, the system demonstrates notable versatility by successfully enabling the dehydrogenative coupling and polymerization of amino acid derivatives, broadening its applicability to a diverse range of substrates.

Notably, our photocatalytic system matches or even surpasses typical homogeneous catalysts in both activity and selectivity.[51,52] This, combined with the recyclable nature of the ZIS NCs, further highlights its potential as a competitive and sustainable alternative for green photocatalysis. Our ongoing research aims to further elucidate the underlying photocatalytic mechanism of ZIS NCs, paving the way for innovative advancements in sustainable synthesis and green chemical transformations.

Data availability

Supplementary notes, synthetic procedures, NMR spectra (Fig. S38-S65), GC traces and characterization setup and data are available within this article and its Supplementary Information. The X-ray crystallographic coordinates for structures reported in this article have been deposited at the Cambridge Crystallographic Data Centre (CCDC), under deposition numbers CCDC 2432269 The data can be obtained free of charge from The Cambridge Crystallographic Data Centre via http://www.ccdc.cam.ac.uk/data_request/cif. Any further relevant data are available from the authors upon reasonable request.

References

1. Lv, J. *et al.* Solar utilization beyond photosynthesis. *Nat. Rev. Chem.* **7**, 91-105, doi:10.1038/s41570-022-00448-9 (2023).
2. Dogutan, D. K. & Nocera, D. G. Artificial photosynthesis at efficiencies greatly exceeding that of natural photosynthesis. *Acc. Chem. Res.* **52**, 3143-3148, doi:10.1021/acs.accounts.9b00380 (2019).
3. Whittingham, M. S. Electrical energy storage and intercalation chemistry. *Science* **192**, 1126-1127, doi:10.1126/science.192.4244.1126 (1976).
4. Zhang, L. *et al.* Tracking the chemical and structural evolution of the TiS_2 electrode in the lithium-ion cell using *operando* X-ray absorption spectroscopy. *Nano Lett.* **18**, 4506-4515, doi:10.1021/acs.nanolett.8b01680 (2018).
5. Savateev, O. Photocharging of semiconductor materials: Database, quantitative data analysis, and application in organic synthesis. *Advanced Energy Materials* **12**, doi:10.1002/aenm.202200352 (2022).
6. Rogolino, A. & Savateev, O. Photochargeable semiconductors: in "Dark photocatalysis" and beyond. *Adv. Funct. Mater.* **33**, 2305028, doi:10.1002/adfm.202305028 (2023).
7. Lau, V. W. *et al.* Dark photocatalysis: Storage of solar energy in carbon nitride for time-delayed hydrogen generation. *Angew. Chem. Int. Ed.* **56**, 510-514, doi:10.1002/anie.201608553 (2017).
8. Hou, X. *et al.* Engineering Auger recombination in colloidal quantum dots via dielectric screening. *Nat. Commun.* **10**, 1750, doi:10.1038/s41467-019-09737-2 (2019).
9. Loh, J. Y. Y., Kherani, N. P. & Ozin, G. A. Persistent CO_2 photocatalysis for solar fuels in the dark. *Nat. Sustain.* **4**, 466-473, doi:10.1038/s41893-021-00681-y (2021).
10. Gallagher, J. Photocatalysis: Into the dark. *Nat. Energy* **2**, doi:10.1038/nenergy.2016.211 (2017).
11. Zhang, P., Wang, T., Chang, X. & Gong, J. Effective charge carrier utilization in photocatalytic conversions. *Acc. Chem. Res.* **49**, 911-921, doi:10.1021/acs.accounts.6b00036 (2016).
12. Jayasinghe, L., Wei, J., Kim, J., Lineberry, E. & Yang, P. Particle on a rod: Surface-tethered catalyst on CdS nanorods for enzymatically active nicotinamide cofactor generation. *Nano Lett.* **24**, 13269-13276, doi:10.1021/acs.nanolett.4c03528 (2024).
13. Panchal, U., Chaudhary, M. L., Patel, P., Patel, J. & Gupta, R. K. Soybean-based bio-adhesives: Role of diamine on the adhesive properties. *ACS Omega* **9**, 10738-10747, doi:10.1021/acsomega.3c09650 (2024).
14. Błażek, K., Kasprzyk, P. & Datta, J. Diamine derivatives of dimerized fatty acids and bio-based polyether polyol as sustainable platforms for the synthesis of non-isocyanate polyurethanes. *Polymer* **205**, 122768, doi:10.1016/j.polymer.2020.122768 (2020).
15. Nakajima, M., Fava, E., Loescher, S., Jiang, Z. & Rueping, M. Photoredox-catalyzed reductive coupling of aldehydes, ketones, and imines with visible light. *Angew. Chem. Int. Ed.* **54**, 8828-8832, doi:10.1002/anie.201501556 (2015).
16. Ma, W., Liu, Y., Yu, N. & Yan, K. Solvent-free mechanochemical diaza-Cope rearrangement. *ACS Sustain. Chem. Eng.* **9**, 16092-16102, doi:10.1021/acssuschemeng.1c04459 (2021).
17. Qi, M. Y., Conte, M., Anpo, M., Tang, Z. R. & Xu, Y. J. Cooperative coupling of oxidative organic synthesis and hydrogen production over semiconductor-based photocatalysts. *Chem. Rev.* **121**, 13051-13085, doi:10.1021/acs.chemrev.1c00197 (2021).
18. Li, X. B. *et al.* Semiconductor nanocrystals for small molecule activation via artificial photosynthesis. *Chem. Soc. Rev.* **49**, 9028-9056, doi:10.1039/d0cs00930j (2020).
19. Park, S., Choi, S., Kim, S. & Nam, K. T. Metal halide perovskites for solar fuel production and photoreactions. *J. Phys. Chem. Lett.* **12**, 8292-8301, doi:10.1021/acs.jpclett.1c02373 (2021).
20. Martin, J. S. *et al.* A nanocrystal catalyst incorporating a surface bound transition metal to induce photocatalytic sequential electron transfer events. *J. Am. Chem. Soc.* **143**, 11361-11369, doi:10.1021/jacs.1c00503 (2021).
21. Huang, Y. *et al.* Photoimmobilized Ni clusters boost photodehydrogenative coupling of amines to imines via enhanced hydrogen evolution kinetics. *ACS Catal.* **10**, 3904-3910, doi:10.1021/acscatal.0c00282 (2020).
22. Qin, Y., Li, J., Chen, L., Lin, S. & Li, Z. Efficient visible-light-initiated dehydrogenative coupling of amines for coproduction of imines and hydrogen over $NiS/ZnIn_2S_4$. *Sol. RRL* **7**, doi:10.1002/solr.202200966 (2022).
23. Liu, X. *et al.* Optimizing the reaction pathway by active site regulation in the CdS/Fe_2O_3 Z-scheme heterojunction system for highly selective photocatalytic benzylamine oxidation integrated with H_2 production. *ACS Catal.* **12**, 12386-12397, doi:10.1021/acscatal.2c03550 (2022).
24. Qi, M. Y., Conte, M., Tang, Z. R. & Xu, Y. J. Engineering semiconductor quantum dots for selectivity switch on high-performance heterogeneous coupling photosynthesis. *ACS Nano* **16**, 17444-17453, doi:10.1021/acsnano.2c08652 (2022).
25. Leng, X. *et al.* Wavelength-selective C–C and C–N bond formation via defect-engineered $ZnIn_2S_4$. *ACS Catal.* **14**, 11554-11563, doi:10.1021/acscatal.4c02199 (2024).
26. Luo, J. *et al.* Photocatalytic methanol dehydrogenation with switchable selectivity. *J. Am. Chem. Soc.* **147**, 3428-3437, doi:10.1021/jacs.4c14413 (2025).
27. Balizer, E. & Duffy, J. V. The effects of steric hindrance on sub-glass transitions in epoxy polymers. *Polymer* **33**, 2114-2122, doi:10.1016/0032-3861(92)90877-y (1992).
28. Grubb, T. L. *et al.* Highly soluble polyimides from sterically hindered diamines. *Polymer* **40**, 4279-4288, doi:10.1016/s0032-3861(98)00663-6 (1999).

29. Liu, P., Xiang, L., Tan, Q., Tang, H. & Zhang, H. Steric hindrance effect on thermoresponsive behaviors of pyrrolidone-based polymers. *Polym. Chem.* **4**, 1068-1076, doi:10.1039/c2py20773g (2013).
30. Shen, R. *et al.* Ni-based photocatalytic H_2-production cocatalysts2. *Chin. J. Catal.* **40**, 240-288, doi:10.1016/s1872-2067(19)63294-8 (2019).
31. Wenderich, K. & Mul, G. Methods, mechanism, and applications of photodeposition in photocatalysis: A review. *Chem. Rev.* **116**, 14587-14619, doi:10.1021/acs.chemrev.6b00327 (2016).
32. Wang, M. *et al.* Photocatalytic coupling of amines to imidazoles using a Mo-$ZnIn_2S_4$ catalyst. *Green Chem.* **19**, 5172-5177, doi:10.1039/c7gc01728f (2017).
33. Ghini, M. *et al.* Control of electronic band profiles through depletion layer engineering in core–shell nanocrystals. *Nature Communications* **13**, doi:10.1038/s41467-022-28140-y (2022).
34. Wang, C., Shim, M. & Guyot-Sionnest, P. Electrochromic nanocrystal quantum dots. *Science* **291**, 2390-2392, doi:10.1126/science.291.5512.2390 (2001).
35. Shulenberger, K. E., Keller, H. R., Pellows, L. M., Brown, N. L. & Dukovic, G. Photocharging of colloidal CdS nanocrystals. *J. Phys. Chem. C* **125**, 22650-22659, doi:10.1021/acs.jpcc.1c06491 (2021).
36. Homer, M. K. *et al.* Extremely Long-lived charge donor states formed by visible irradiation of quantum dots. *ACS Nano* **18**, 24591-24602, doi:10.1021/acsnano.4c10526 (2024).
37. Rinehart, J. D., Schimpf, A. M., Weaver, A. L., Cohn, A. W. & Gamelin, D. R. Photochemical electronic doping of colloidal CdSe nanocrystals. *J. Am. Chem. Soc.* **135**, 18782-18785, doi:10.1021/ja410825c (2013).
38. Shim, M., Wang, C. & Guyot-Sionnest, P. Charge-tunable optical properties in colloidal semiconductor nanocrystals. *J. Phys. Chem. B* **105**, 2369-2373, doi:10.1021/jp0035683 (2001).
39. Giansante, C. & Infante, I. Surface traps in colloidal quantum dots: A combined experimental and theoretical perspective. *J. Phys. Chem. Lett.* **8**, 5209-5215, doi:10.1021/acs.jpclett.7b02193 (2017).
40. Peng, H. *et al.* Defective $ZnIn_2S_4$ Nanosheets for visible-light and sacrificial-Agent-Free H_2O_2 Photosynthesis via O_2/H_2O Redox. *J. Am. Chem. Soc.* **145**, 27757-27766, doi:10.1021/jacs.3c10390 (2023).
41. Wang, X. *et al.* Interfacial chemical bond and internal electric field modulated Z-scheme S_v- $ZnIn_2S_4$/$MoSe_2$ photocatalyst for efficient hydrogen evolution. *Nat. Commun.* **12**, 4112, doi:10.1038/s41467-021-24511-z (2021).
42. Chi, L. P. *et al.* Stabilizing indium sulfide for CO_2 electroreduction to formate at high rate by zinc incorporation. *Nat. Commun.* **12**, 5835, doi:10.1038/s41467-021-26124-y (2021).
43. Voznyy, O., Thon, S. M., Ip, A. H. & Sargent, E. H. Dynamic trap formation and elimination in colloidal quantum dots. *J. Phys. Chem. Lett.* **4**, 987-992, doi:10.1021/jz400125r (2013).
44. Wang, G. *et al.* Synthesis and characterization of ZnS with controlled amount of S vacancies for photocatalytic H_2 production under visible light. *Sci. Rep.* **5**, 8544, doi:10.1038/srep08544 (2015).
45. Wang, Y. *et al.* Decoupling of light and dark reactions in a 2D niobium tungstate for light-induced charge storage and on-demand hydrogen evolution. *J. Am. Chem. Soc.* **146**, 25467-25476, doi:10.1021/jacs.4c04140 (2024).
46. Hu, W. *et al.* Proton–electron-coupled MoS_2 synaptic transistors with a natural renewable biopolymer neurotransmitter for brain-inspired neuromorphic learning. *J. Mater. Chem. C* **7**, 682-691, doi:10.1039/c8tc04740e (2019).
47. Ritter, C. Location of hydrogen in intercalation compounds of layered transition metal disulfides, a ^{1}H NMR study. *Solid State Ion.* **20**, 283-289, doi:10.1016/0167-2738(86)90047-0 (1986).
48. Gao, Z. *et al.* Hydrogen bonding promotes alcohol C-C coupling. *J. Am. Chem. Soc.* **144**, 18986-18994, doi:10.1021/jacs.2c07410 (2022).
49. Jiang, Y., Wang, C., Rogers, C. R., Kodaimati, M. S. & Weiss, E. A. Regio- and diastereoselective intermolecular [2+2] cycloadditions photocatalysed by quantum dots. *Nat. Chem.* **11**, 1034-1040, doi:10.1038/s41557-019-0344-4 (2019).
50. Beatty, J. W. & Stephenson, C. R. Amine functionalization via oxidative photoredox catalysis: Methodology development and complex molecule synthesis. *Acc. Chem. Res.* **48**, 1474-1484, doi:10.1021/acs.accounts.5b00068 (2015).
51. Ohmatsu, K. & Ooi, T. Catalytic acceptorless dehydrogenative coupling mediated by photoinduced hydrogen-atom transfer. *Nat. Synth.* **2**, 209-216, doi:10.1038/s44160-022-00195-1 (2023).
52. Gunanathan, C. & Milstein, D. Applications of acceptorless dehydrogenation and related transformations in chemical synthesis. *Science* **341**, 1229712, doi:10.1126/science.1229712 (2013).

Acknowledgements

This work was financially supported by the BASF CARA program (No. 051355). VB-XPS measurements and Electron microscopy are carried out at the Molecular Foundry at Lawrence Berkeley National Lab (LBNL), supported by the Office of Science, Office of Basic Energy Sciences, of the U.S. Department of Energy under Contract No. DE-AC02-05CH11231. We thank Drs. Hasan Celik, Raynald Giovine, and Pines Magnetic Resonance Center's Core NMR Facility (PMRC Core) for spectroscopic assistance. The instruments used in this work were supported by the PMRC Core. J.L. and L.J. thank Patrick W. Smith for his assistance with the EPR measurements. Work performed at the Center for Nanoscale Materials, a U.S. Department of Energy Office of Science User Facility, was supported by the U.S. DOE, Office of Basic Energy Sciences, under Contract No. DE-AC02-06CH11357. We thank Chris Pollock and Chris Mobley from Cornell High Energy Synchrotron Source (CHESS) for their help with XAS experiments.

Author contributions

P.Y. supervised the project. P.Y., J.L., and B.S. conceived and directed the project. J.L. conducted the particle synthesis, photocatalytic reactions, and coordinated the mechanistic studies and designed the experiments with X.C. and L.J.. X.C. led the *operando* XAS experiments and EXAFS fitting with N.E.S., J.H., and J.F., and performed catalytic experiments and analysis with K.M.D.. L.J. performed the EPR measurements and simulations, carried out the kinetic and time-resolved analyses, titration experiments and completed the TA data analysis. R.D.S. conducted the TA measurements and provided feedback on the analysis. N.E.S performed *in situ* XAS experiments on Ni. H.Z. analyzed the XRD data, including SCXRD and PXRD. A.L.M., Y.S., M.F.G. and N.E.S carried out the EDS, XPS, Raman, photoelectrochemical measurements, respectively. A.M.D. provided valuable suggestions and discussions regarding the materials. X.C. and K.M.D. repeated selected experiments. B.S., M.S., R.Z., and C.L. Pueyo contributed insightful discussions on the development and objectives of the project. J.L. drafted the manuscript with input from all authors.

Additional information

Supplementary information and chemical compound information are available in the online version of the paper. Reprints and permissions information is available online at www.nature.com/reprints. Publisher's note: Springer Nature remains neutral with regard to jurisdictional claims in published maps and institutional affiliations. Correspondence and requests for materials should be addressed to P.Y.

Competing interests

P.Y., J.L., B.S., M.S., R.Z., F.S., and C.L. are listed as inventors on a provisional patent application related to this work. All other coauthors declare no competing interests.

Methods

Colloidal synthesis of ZIS NCs:

$ZnCl_2$ (138 mg, 1 mmol), $InCl_3$ (147 mg, 0.66 mmol), and trioctylphosphine oxide (2.3 g, TOPO) were added to a 50 mL three-neck flask in a glovebox. The flask was then removed from the glovebox, and 10 mL of oleylamine (OAm) was quickly added. The mixture was heated to 120 °C under vacuum for 60 minutes with stirring at 650 rpm, then further heated to an internal temperature of 220 °C. Sulfur (51.2 mg, 1.6 mmol, in 2 mL OAm) was then quickly injected, causing an immediate color change from light yellow to dark red, which gradually shifted to orange-yellow upon continued heating at 220 °C for 1 hour. The mixture was then cooled to room temperature, followed by the addition of 30 mL ethanol. The precipitate was collected by centrifugation at 12,000 rpm for 5 minutes and redissolved in toluene (10 mL). This solution was centrifuged again at 12,000 rpm for 10 minutes, and the supernatant was collected. The composition of the resulting ZIS NCs was determined by ICP as $Zn_{1.4}In_2S_x$ after sonicating in aqua regia overnight.

Ligand exchange:

The hydrophobic native surface-capping ligands of the as-synthesized ZIS NCs were replaced with inorganic sulfide (S^{2-}) ligands following a previously reported procedure. Briefly, an aliquot of the native ligand-capped ZIS NRs (10 mg, ~300 µL in toluene) was added to a solution of $(NH_4)_2S$ (8 µL, 50% aqueous solution) in 5 mL *N*-methylformamide (NMF), and the resulting suspension was stirred at room temperature for 20 minutes. Toluene (35 mL) was then added, and the mixture was centrifuged at 12,000 rpm for 5 minutes. The solid was collected, washed twice with toluene (3 mL each), quickly rinsed once with DMF (3 mL), and then redispersed in 5 mL DMF.

Gram-scale preparation of ZIS NCs

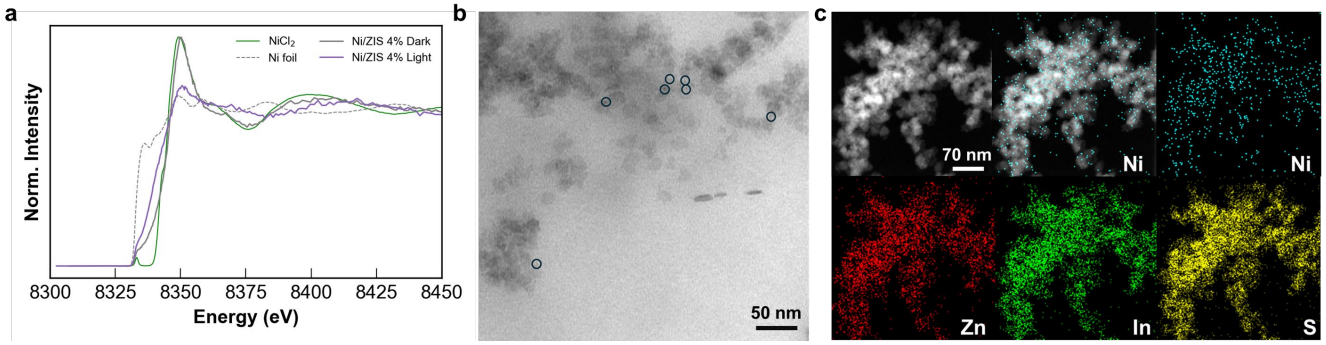
$ZnCl_2$ (1.38 g, 10 mmol), $InCl_3$ (1.47 g, 6.6 mmol), and trioctylphosphine oxide (23 g, TOPO) were added to a 250 mL three-neck flask in a glovebox. The flask was then removed from the glovebox, and 100 mL of oleylamine (OAm) was quickly added. The mixture was heated to 120 °C under vacuum for 60 minutes with stirring at 300 rpm, then further heated to an internal temperature of 220 °C. Sulfur (0.51 g, 16 mmol, in 20 mL OAm) was quickly injected, causing an immediate color change from light yellow to dark red, which gradually shifted to orange-yellow upon continued heating at 220 °C for 1 hour. The mixture was cooled to room temperature, followed by the addition of 300 mL ethanol. The precipitate was collected by centrifugation at 12,000 rpm for 5 minutes and redissolved in toluene (60 mL). This solution was centrifuged again at 12,000 rpm for 10 minutes, and the supernatant was collected. The composition of the resulting ZIS NCs was determined by ICP as $Zn_{1.5}In_2S_x$ after sonication in aqua regia overnight. Size screening for TEM imaging was performed using ethanol as the antisolvent.

Photocatalytic dehydrogenative coupling of amines (gram scale):

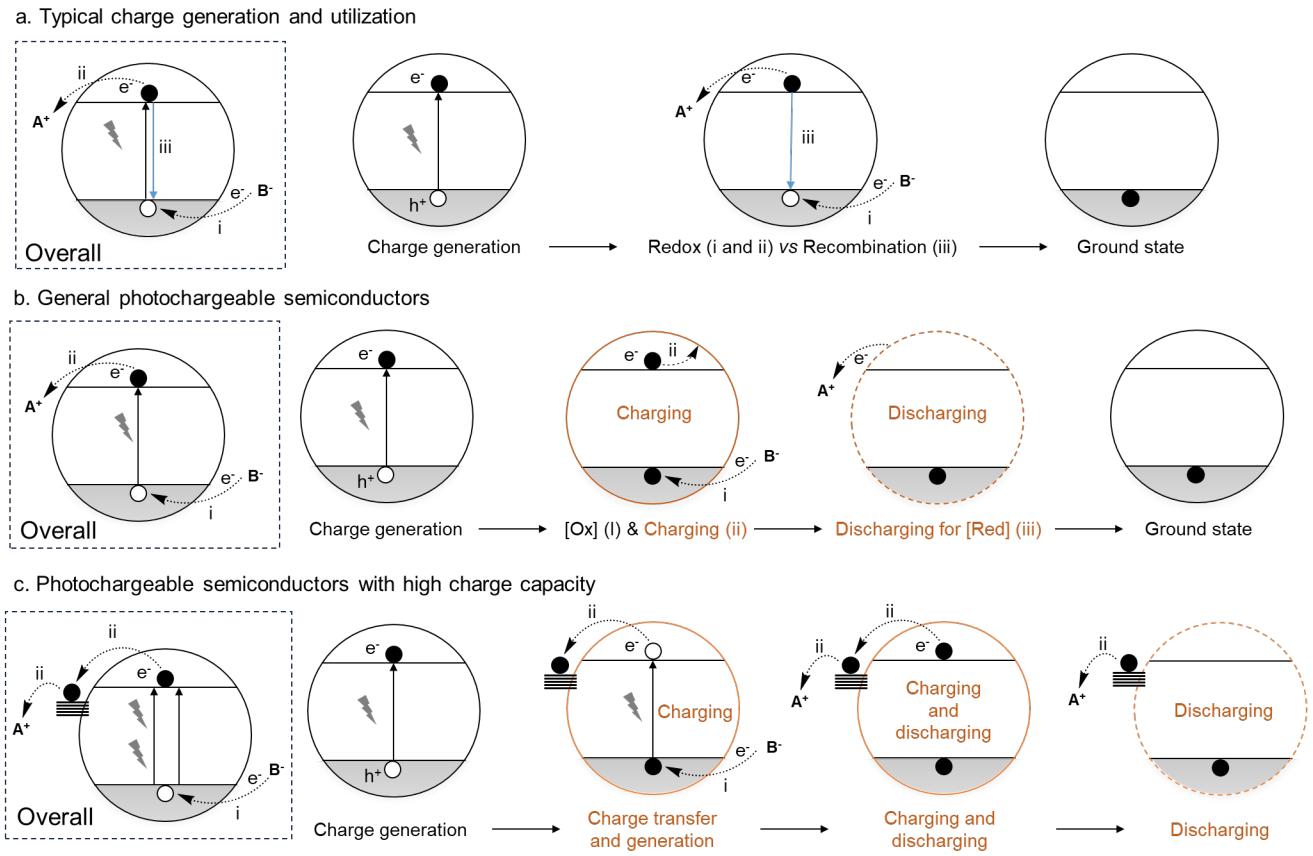
A clear dispersion of ZIS NCs (2 mg in 1 mL DMF), $NiCl_2{\cdot}6H_2O$ (60 µg Ni, 3 wt%, in 120 µL stock solution in DMF), amine **1** (1 mL or 1 g), and DMF (3 mL) were added to a 30 mL quartz tube (1.5 cm diameter). The tube was capped with an adaptor equipped with a three-way valve, purged with argon, and then exposed to 370 nm light from a Kessil lamp at an intensity of 30 mW/cm^2 for a specified duration. A fan was used to maintain room temperature throughout the reaction. The generated gas was analyzed by GC, and the crude reaction mixture was measured by NMR with ethyl acetate as an internal standard.

Photocatalytic dehydrogenative coupling of amines (20 grams scale):

A clear dispersion of ZIS NCs (40 mg in 20 mL DMF), $NiCl_2{\cdot}6H_2O$ (1.2 mg Ni, 3 wt%, in 2.4 mL stock solution in DMF), amine **1** (either 20 mL of α-methylbenzylamine **1a** or 21.6 g alanine ester **1h**), and DMF (60 mL) were added to a 350 mL quartz tube (5 cm diameter). The tube was sealed with an adaptor, purged with argon, and connected to an inverted gas cylinder refilled with water. The reaction mixture was exposed to 370 nm light from a Kessil lamp at an intensity of 40±10 mW/cm^2 (variation of the intensity due to the bigger diameter of the tube) for 36 hours (for alanine ester) or 45 hours (for α-methylbenzylamine), with a fan maintaining room temperature throughout the reaction. The collected gas was analyzed by GC, and the crude reaction mixture was measured by NMR with ethyl acetate as an internal standard to determine the selectivity. For workup, ethyl acetate (150 mL) was added to the mixture, and the solution was washed with brine (4 × 100 mL). The organic phases were dried over anhydrous Na_2SO_4, and solvent removal afforded the diamine product with NMR purity.



Extended data Fig. 1 | Characterization of Ni cocatalyst. **a**, *In situ* Ni K-edge XANES spectra of the photocatalyst before and after UV irradiation, shown alongside Ni foil and $NiCl_2$ standards (the cocatalyst precursor). Upon illumination, the rising edge shifts to lower energy and the white-line intensity decreases, indicating an average reduction of Ni species and increased filling of Ni 3d states. The post-edge oscillations differ from those of Ni foil, likely reflecting the low coordination environment of photodeposited Ni and reduced Ni–Ni scattering. These *in situ* results are consistent with *ex situ* post-catalysis observations showing the formation of Ni nanoparticles on the ZIS surface and XPS evidence for partial Ni^0 formation. **b**, TEM image of ZIS nanocrystals loaded with 6 wt% Ni. The black spots highlighted in the image correspond to Ni nanoparticles. **c**, High-angle annular dark-field scanning transmission electron microscopy (HAADF-STEM) and the corresponding elemental mapping after reaction further confirm the homogeneous distribution of Zn, In, S, and Ni across the nanocrystals.

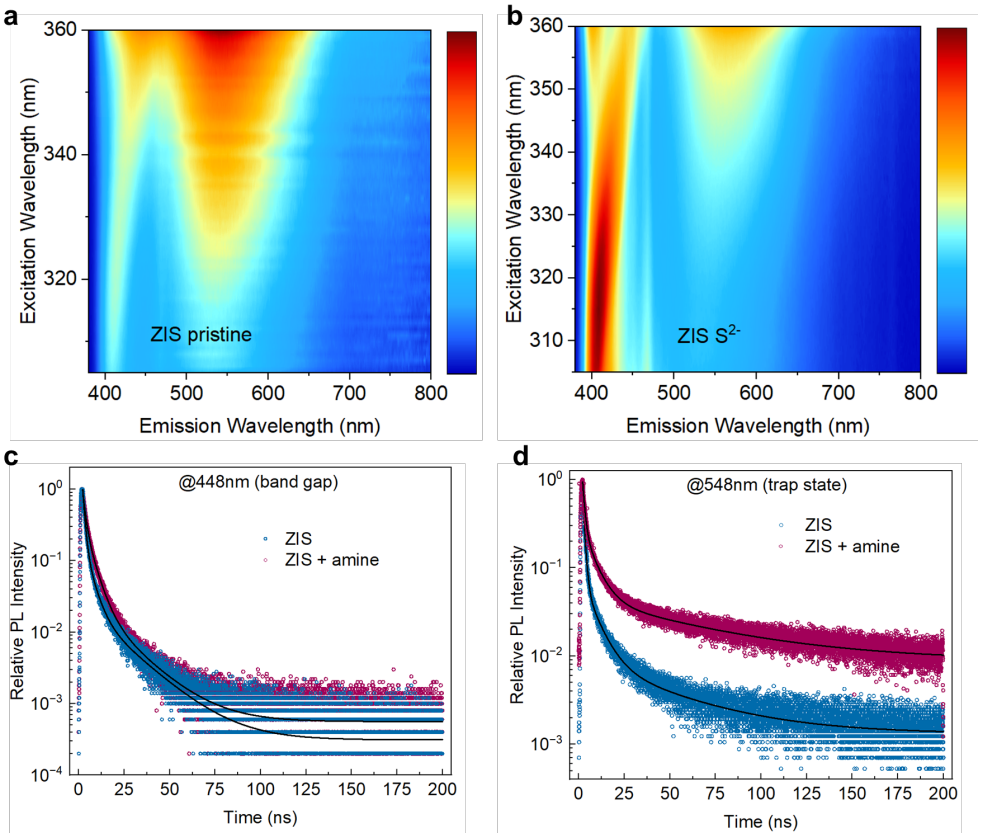


Extended data Fig. 2 | Schematic representation of charge utilization in photochargeable semiconductors. a, Charge utilization in typical semiconductors, where charge recombination competes with charge transfer, limiting the efficiency of redox chemical reactions. **b,** Charge utilization in photochargeable semiconductors, featuring decoupled electron and hole pathways, which enhance charge utilization efficiency by minimizing charge recombination. However, the saturation of the conduction band prohibits further photon absorption. **c,** Photochargeable semiconductors with high charge capacity enable enhanced light absorption, facilitated by effective electron trapping mechanisms.

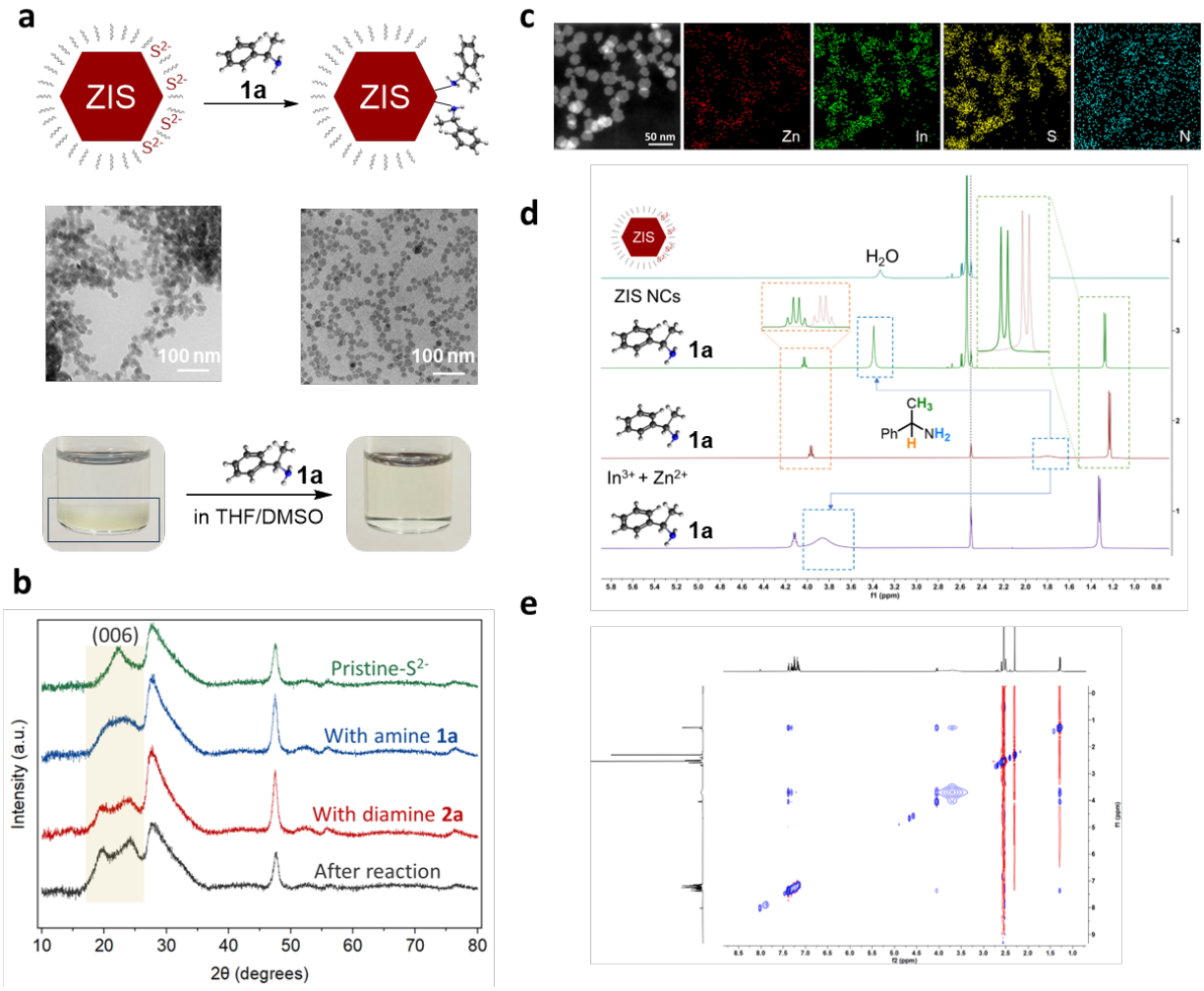
Extended data Table 1. | EXAFS Curvefit Parameters[a] for ZIS_Dark, ZIS_light on 90 min and ZIS_light off 90 min at the Zn K-edge and the In K-edge. At the In K-edge, quantitative fitting shows that the coordination number decreases from 6 $(In–S)_1$ bonds and 4 $(In–S)_2$ bonds in the dark to 3.6 and 2.4, respectively, under illumination—corresponding to roughly a 40% loss of total In–S coordination. This substantial decrease indicates significant weakening or cleavage of surface In–S bonds during photocharging. When the light is turned off, the In–S coordination partially recovers (4.5 and 3.0), showing that ~15% of this structural change is reversible while the remainder reflects persistent surface reconstruction under photocatalytic conditions. In contrast, the Zn K-edge EXAFS remains essentially unchanged, consistent with Zn occupying more bulk-like tetrahedral environments, whereas the surface-exposed In sites undergo stronger photoinduced distortions.

Sample	Path	N[b]	(*R* / Å) [c]	(σ^2 / Å^2)[d]	R-factor[e]
ZIS_Dark	Zn-S	4	2.33(1)	0.006(1)	1.1%
	$(In-S)_1$	6	2.47(3)	0.010(4)	1.7%
	$(In-S)_2$	4	2.62(3)	0.009(9)	1.7%
ZIS_light 90 min	Zn-S	4.0(0)	2.33(1)	0.006(1)	1.1%
	$(In-S)_1$	3.6(13)	2.44(0)	0.003(9)	1.0%
	$(In-S)_2$	2.4(9)	2.61(3)	0.001(11)	1.0%
ZIS_light off 90 min	Zn-S	4.0(3)	2.33(1)	0.006(1)	0.9%
	$(In-S)_1$	4.5(12)	2.45(0)	0.007(6)	0.5%
	$(In-S)_2$	3.0(8)	2.61(3)	0.004(8)	0.5%

[a] S_0^2 was fixed to 0.918 and 0.7 respectively, according to the experimental EXAFS fit of ZIS_Dark at the Zn K-edge and the In K-edge by fixing *N* as the known crystallographic value of $Zn_2In_2S_5$. [b]N, coordination number; [c]R, the distance to the neighboring atom; [d]σ^2, Debye-Waller factor, the Mean Square Relative Displacement (MSRD); [e] A reasonable range of EXAFS fitting parameters: $0.700 \le S_0^2 \le 1.000$; N > 0; $0.001 \le \sigma^2 \le 0.01$ Å^2; $|\Delta E_0| \le 5$ eV; R-factor ≤ 2.0%. More parameters and optimization details are provided in the Supporting Information



Extended data Fig. 3 |Photoluminescence study. a Photoluminescence excitation contour plots of pristine ZIS collected (a) and ZIS-S2- after ligand exchange by monitoring emission at 448 nm (band-edge channel) and 548 nm (trap-state channel). Time-resolved photoluminescence decay profiles of ZIS (a) and ZIS in the presence of amine (b) monitored at 448 nm and 548 nm. Pristine ZIS exhibits two characteristic emission channels: a band-edge emission centered at 448 nm and a lower-energy trap-state emission at 548 nm. The TRPL decay profiles reveal that the 448 nm band-edge emission decays rapidly within tens of nanoseconds, consistent with fast recombination of shallowly localized carriers. In contrast, the 548 nm trap-state emission displays a significantly longer lifetime, reflecting recombination from deeply trapped electrons. Upon amine treatment, both emission channels become longer-lived, but the effect is particularly pronounced for the 548 nm trap-state decay. This behavior indicates that amines further stabilize trapped electrons and suppress their recombination, consistent with the TA-derived conclusion that amines slow down GSB recovery by consuming photogenerated holes and extending electron lifetimes.



Extended data Fig. 4 | Studies on ZIS NCs with amine reactant serving as surface ligand. a, Interaction of amines to the surface of the ZIS NCs. ZIS NCs disperse well in a DMSO-THF solvent mixture, forming a clear solution in the presence of amine, unlike in the absence of amines where they tend to precipitate, as indicated in the relevant TEM images (left, ZIS NCs in water; right, ZIS NCs in DMF in the presence of amine). **b**, Powder XRD pattern of pristine ZIS NCs, ZIS NCs after the treatment of amine and diamine, and the ZIS NCs after reaction. The (006) plane of ZIS NCs exhibited a shift in the presence of either the starting amine or the diamine product. This shift was also detected in ZIS nanocrystals collected after the photocatalytic reaction, indicating consistent surface interactions between the amines and the catalyst throughout the reaction process. **c**, High-angle annular dark-field scanning transmission electron microscopy (HAADF-STEM) and the corresponding element mapping of the ZIS NCs after the addition of amines. ZIS nanoplates primarily exist as single layers rather than aggregated structures, suggesting stabilization by amine ligands. The nitrogen distribution may be partially affected by beam damage, causing some detachment or scattering of the organic ligands. **d**, ^{1}H NMR studies of amine protons upon mixing with ZIS NCs show a downfield shift of the amine peaks while retaining sharpness rather than broadening, suggesting that amines bind tightly to the ZIS surface. **e,** ^{1}H - ^{1}H NOESY spectrum of 5 μL α-methylbenzylamine **1a** and 2 mg ZIS NCs in DMSO-d_6. The observed cross-signals between the protons of **1a** indicate a clear nuclear Overhauser effect (NOE), suggesting their spatial proximity and interaction to the surface of the ZIS NCs.

1 Lv, J. *et al.* Solar utilization beyond photosynthesis. *Nat Rev Chem* **7**, 91-105, doi:10.1038/s41570-022-00448-9 (2023).

2 Dogutan, D. K. & Nocera, D. G. Artificial Photosynthesis at Efficiencies Greatly Exceeding That of Natural Photosynthesis. *Acc Chem Res* **52**, 3143-3148, doi:10.1021/acs.accounts.9b00380 (2019).

3 Whittingham, M. S. Electrical Energy Storage and Intercalation Chemistry. *Science* **192**, 1126-1127, doi:10.1126/science.192.4244.1126 (1976).

4 Zhang, L. *et al.* Tracking the Chemical and Structural Evolution of the TiS2 Electrode in the Lithium-Ion Cell Using Operando X-ray Absorption Spectroscopy. *Nano Letters* **18**, 4506-4515, doi:10.1021/acs.nanolett.8b01680 (2018).

5 Savateev, O. Photocharging of Semiconductor Materials: Database, Quantitative Data Analysis, and Application in Organic Synthesis. *Advanced Energy Materials* **12**, doi:10.1002/aenm.202200352 (2022).

6 Rogolino, A. & Savateev, O. Photochargeable Semiconductors: in “Dark Photocatalysis” and Beyond. *Advanced Functional Materials* **33**, doi:10.1002/adfm.202305028 (2023).

7 Lau, V. W. *et al.* Dark Photocatalysis: Storage of Solar Energy in Carbon Nitride for Time-Delayed Hydrogen Generation. *Angew Chem Int Ed Engl* **56**, 510-514, doi:10.1002/anie.201608553 (2017).

8 Hou, X. *et al.* Engineering Auger recombination in colloidal quantum dots via dielectric screening. *Nat Commun* **10**, 1750, doi:10.1038/s41467-019-09737-2 (2019).

9 Loh, J. Y. Y., Kherani, N. P. & Ozin, G. A. Persistent CO2 photocatalysis for solar fuels in the dark. *Nature Sustainability* **4**, 466-473, doi:10.1038/s41893-021-00681-y (2021).

10 Gallagher, J. Photocatalysis: Into the dark. *Nature Energy* **2**, doi:10.1038/nenergy.2016.211 (2017).

11 Zhang, P., Wang, T., Chang, X. & Gong, J. Effective Charge Carrier Utilization in Photocatalytic Conversions. *Acc Chem Res* **49**, 911-921, doi:10.1021/acs.accounts.6b00036 (2016).

12 Jayasinghe, L., Wei, J., Kim, J., Lineberry, E. & Yang, P. Particle on a Rod: Surface-Tethered Catalyst on CdS Nanorods for Enzymatically Active Nicotinamide Cofactor Generation. *Nano Lett* **24**, 13269-13276, doi:10.1021/acs.nanolett.4c03528 (2024).

13 Panchal, U., Chaudhary, M. L., Patel, P., Patel, J. & Gupta, R. K. Soybean Oil-Based Bio-Adhesives: Role of Diamine on the Adhesive Properties. *ACS Omega* **9**, 10738-10747, doi:10.1021/acsomega.3c09650 (2024).

14 Błażek, K., Kasprzyk, P. & Datta, J. Diamine derivatives of dimerized fatty acids and bio-based polyether polyol as sustainable platforms for the synthesis of non-isocyanate polyurethanes. *Polymer* **205**, doi:10.1016/j.polymer.2020.122768 (2020).

15 Nakajima, M., Fava, E., Loescher, S., Jiang, Z. & Rueping, M. Photoredox-Catalyzed Reductive Coupling of Aldehydes, Ketones, and Imines with Visible Light. *Angew Chem Int Ed Engl* **54**, 8828-8832, doi:10.1002/anie.201501556 (2015).

16 Ma, W., Liu, Y., Yu, N. & Yan, K. Solvent-Free Mechanochemical Diaza-Cope Rearrangement. *ACS Sustainable Chemistry & Engineering* **9**, 16092-16102, doi:10.1021/acssuschemeng.1c04459 (2021).

17 Qi, M. Y., Conte, M., Anpo, M., Tang, Z. R. & Xu, Y. J. Cooperative Coupling of Oxidative Organic Synthesis and Hydrogen Production over Semiconductor-Based Photocatalysts. *Chem Rev* **121**, 13051-13085, doi:10.1021/acs.chemrev.1c00197 (2021).

18 Li, X. B. *et al.* Semiconductor nanocrystals for small molecule activation via artificial photosynthesis. *Chem Soc Rev* **49**, 9028-9056, doi:10.1039/d0cs00930j (2020).

19 Park, S., Choi, S., Kim, S. & Nam, K. T. Metal Halide Perovskites for Solar Fuel Production and Photoreactions. *The Journal of Physical Chemistry Letters* **12**, 8292-8301, doi:10.1021/acs.jpclett.1c02373 (2021).

20 Martin, J. S. *et al.* A Nanocrystal Catalyst Incorporating a Surface Bound Transition Metal to Induce Photocatalytic Sequential Electron Transfer Events. *Journal of the American Chemical Society* **143**, 11361-11369, doi:10.1021/jacs.1c00503 (2021).
21 Huang, Y. *et al.* Photoimmobilized Ni Clusters Boost Photodehydrogenative Coupling of Amines to Imines via Enhanced Hydrogen Evolution Kinetics. *ACS Catalysis* **10**, 3904-3910, doi:10.1021/acscatal.0c00282 (2020).
22 Qin, Y., Li, J., Chen, L., Lin, S. & Li, Z. Efficient Visible‐Light‐Initiated Dehydrogenative Coupling of Amines for Coproduction of Imines and Hydrogen over NiS/ZnIn2S4. *Solar RRL* **7**, doi:10.1002/solr.202200966 (2022).
23 Liu, X. *et al.* Optimizing the Reaction Pathway by Active Site Regulation in the CdS/Fe2O3 Z-Scheme Heterojunction System for Highly Selective Photocatalytic Benzylamine Oxidation Integrated with H2 Production. *ACS Catalysis* **12**, 12386-12397, doi:10.1021/acscatal.2c03550 (2022).
24 Qi, M. Y., Conte, M., Tang, Z. R. & Xu, Y. J. Engineering Semiconductor Quantum Dots for Selectivity Switch on High-Performance Heterogeneous Coupling Photosynthesis. *ACS Nano* **16**, 17444-17453, doi:10.1021/acsnano.2c08652 (2022).
25 Leng, X. *et al.* Wavelength-Selective C–C and C–N Bond Formation via Defect-Engineered ZnIn2S4. *ACS Catalysis* **14**, 11554-11563, doi:10.1021/acscatal.4c02199 (2024).
26 Luo, J. *et al.* Photocatalytic Methanol Dehydrogenation with Switchable Selectivity. *J Am Chem Soc*, doi:10.1021/jacs.4c14413 (2025).
27 Balizer, E. & Duffy, J. V. The effects of steric hindrance on sub-glass transitions in epoxy polymers. *Polymer* **33**, 2114-2122, doi:10.1016/0032-3861(92)90877-y (1992).
28 Grubb, T. L. *et al.* Highly soluble polyimides from sterically hindered diamines. *Polymer* **40**, 4279-4288, doi:10.1016/s0032-3861(98)00663-6 (1999).
29 Liu, P., Xiang, L., Tan, Q., Tang, H. & Zhang, H. Steric hindrance effect on thermoresponsive behaviors of pyrrolidone-based polymers. *Polym. Chem* **4**, 1068-1076, doi:10.1039/c2py20773g (2013).
30 Shen, R. *et al.* Ni-based photocatalytic H2-production cocatalysts2. *Chinese Journal of Catalysis* **40**, 240-288, doi:10.1016/s1872-2067(19)63294-8 (2019).
31 Wenderich, K. & Mul, G. Methods, Mechanism, and Applications of Photodeposition in Photocatalysis: A Review. *Chem Rev* **116**, 14587-14619, doi:10.1021/acs.chemrev.6b00327 (2016).
32 Wang, M. *et al.* Photocatalytic coupling of amines to imidazoles using a Mo–ZnIn2S4 catalyst. *Green Chem* **19**, 5172-5177, doi:10.1039/c7gc01728f (2017).
33 Ghini, M. *et al.* Control of electronic band profiles through depletion layer engineering in core–shell nanocrystals. *Nature Communications* **13**, doi:10.1038/s41467-022-28140-y (2022).
34 Wang, C., Shim, M. & Guyot-Sionnest, P. Electrochromic nanocrystal quantum dots. *Science* **291**, 2390-2392, doi:10.1126/science.291.5512.2390 (2001).
35 Shulenberger, K. E., Keller, H. R., Pellows, L. M., Brown, N. L. & Dukovic, G. Photocharging of Colloidal CdS Nanocrystals. *The Journal of Physical Chemistry C* **125**, 22650-22659, doi:10.1021/acs.jpcc.1c06491 (2021).
36 Homer, M. K. *et al.* Extremely Long-Lived Charge Donor States Formed by Visible Irradiation of Quantum Dots. *ACS Nano* **18**, 24591-24602, doi:10.1021/acsnano.4c10526 (2024).
37 Rinehart, J. D., Schimpf, A. M., Weaver, A. L., Cohn, A. W. & Gamelin, D. R. Photochemical electronic doping of colloidal CdSe nanocrystals. *J Am Chem Soc* **135**, 18782-18785, doi:10.1021/ja410825c (2013).
38 Shim, M., Wang, C. & Guyot-Sionnest, P. Charge-Tunable Optical Properties in Colloidal Semiconductor Nanocrystals. *The Journal of Physical Chemistry B* **105**, 2369-2373, doi:10.1021/jp0035683 (2001).

39 Giansante, C. & Infante, I. Surface Traps in Colloidal Quantum Dots: A Combined Experimental and Theoretical Perspective. *J Phys Chem Lett* **8**, 5209-5215, doi:10.1021/acs.jpclett.7b02193 (2017).
40 Peng, H. *et al.* Defective ZnIn(2)S(4) Nanosheets for Visible-Light and Sacrificial-Agent-Free H(2)O(2) Photosynthesis via O(2)/H(2)O Redox. *J Am Chem Soc* **145**, 27757-27766, doi:10.1021/jacs.3c10390 (2023).
41 Wang, X. *et al.* Interfacial chemical bond and internal electric field modulated Z-scheme S(v)-ZnIn(2)S(4)/MoSe(2) photocatalyst for efficient hydrogen evolution. *Nat Commun* **12**, 4112, doi:10.1038/s41467-021-24511-z (2021).
42 Chi, L. P. *et al.* Stabilizing indium sulfide for CO(2) electroreduction to formate at high rate by zinc incorporation. *Nat Commun* **12**, 5835, doi:10.1038/s41467-021-26124-y (2021).
43 Voznyy, O., Thon, S. M., Ip, A. H. & Sargent, E. H. Dynamic Trap Formation and Elimination in Colloidal Quantum Dots. *J Phys Chem Lett* **4**, 987-992, doi:10.1021/jz400125r (2013).
44 Wang, G. *et al.* Synthesis and characterization of ZnS with controlled amount of S vacancies for photocatalytic H2 production under visible light. *Sci Rep* **5**, 8544, doi:10.1038/srep08544 (2015).
45 Wang, Y. *et al.* Decoupling of Light and Dark Reactions in a 2D Niobium Tungstate for Light-Induced Charge Storage and On-Demand Hydrogen Evolution. *J Am Chem Soc* **146**, 25467-25476, doi:10.1021/jacs.4c04140 (2024).
46 Hu, W. *et al.* Proton-electron-coupled MoS2 synaptic transistors with a natural renewable biopolymer neurotransmitter for brain-inspired neuromorphic learning. *Journal of Materials Chemistry C* **7**, 682-691, doi:10.1039/c8tc04740e (2019).
47 Ritter, C. Location of hydrogen in intercalation compounds of layered transition metal disulfides, A 1H NMR study. *Solid State Ionics* **20**, 283-289, doi:10.1016/0167-2738(86)90047-0 (1986).
48 Gao, Z. *et al.* Hydrogen Bonding Promotes Alcohol-C Coupling. *J Am Chem Soc* **144**, 18986-18994, doi:10.1021/jacs.2c07410 (2022).
49 Jiang, Y., Wang, C., Rogers, C. R., Kodaimati, M. S. & Weiss, E. A. Regio- and diastereoselective intermolecular [2+2] cycloadditions photocatalysed by quantum dots. *Nat Chem* **11**, 1034-1040, doi:10.1038/s41557-019-0344-4 (2019).
50 Beatty, J. W. & Stephenson, C. R. Amine Functionalization via Oxidative Photoredox Catalysis: Methodology Development and Complex Molecule Synthesis. *Acc Chem Res* **48**, 1474-1484, doi:10.1021/acs.accounts.5b00068 (2015).
51 Ohmatsu, K. & Ooi, T. Catalytic acceptorless dehydrogenative coupling mediated by photoinduced hydrogen-atom transfer. *Nature Synthesis* **2**, 209-216, doi:10.1038/s44160-022-00195-1 (2023).
52 Gunanathan, C. & Milstein, D. Applications of acceptorless dehydrogenation and related transformations in chemical synthesis. *Science* **341**, 1229712, doi:10.1126/science.1229712 (2013).